Science & Technology Indonesia

Research Paper

Synthesis, Characterization of Novel Azo Compounds as Corrosion Inhibitors for Carbon Steel in HCl, and Their Theoretical Study

Hanadi M. Jarallah[1], Hawraa Kareem Dhaef[1], Mohammed K. Mohammed[1*], Sadiq M. H. Ismal[1], Ala'a Ali Hussein[1]

[1]*Department of Chemistry, College of Education for Pure Science, University of Basrah, Basrah, 61004, Iraq*
Corresponding author: mohammed.khalaf@uobasrah.edu.iq

Abstract

Two azo compounds were produced, and their chemical properties were validated using spectroscopic methods (mass and ^{1}H NMR). A potential dynamic polarization approach was employed to evaluate the synthesized derivatives as corrosion-reducing materials for carbon steel in a 1 M HCl solution. The derived products, (E)-4-((3-(tert-butyl)-2-hydroxy-5-methoxyphenyl)diazenyl)-N-(5-methylisoxazol-3-yl)benzenesulfonamide (I) and (E)-4-((2-hydroxynaphthalen-1-yl)diazenyl)-N-(5-methylisoxazol-3-yl)benzenesulfonamide (II) achieved 89.9% and 83.02% inhibition rates at 5×10^{-3} M concentrations, Langmuir was aligned with the isotherm adsorptions of these materials. Density functional theory was employed to assess the quantum chemical characteristics of azo-based inhibitors. A conceptual assessment was performed using DFT/B3LYP 6-311+G (d,p) to evaluate the structure of the molecule, its physical and chemical properties, and the electronic factors that impact its inhibitory significance. The DFT outcomes were aligned with the practical records.

Keywords

Azo Compounds, Corrosion Inhibition, Potentiodynamic, Polarization, DFT

1. INTRODUCTION

Corrosion is a significant challenge that restricts the widespread application of metallic materials, particularly in industrial and structural contexts. Corrosion-induced deterioration can significantly impact the durability and safety of metal components, often leading to increased maintenance costs (Dhaif et al., 2022; Guo et al., 2018). This phenomenon typically occurs through electrochemical interactions between metals and their environments, where factors such as acidity, salinity, moisture, and oxygen play a crucial role in accelerating the corrosion process. In particular, iron and its alloys are highly susceptible to corrosion, which adversely affects their chemical, physical, and mechanical properties (Al-Hujaj et al., 2023; Ashoor et al., 2025; Jarallah and Ali, 2025).

To mitigate this issue, researchers have explored various strategies, among which the use of corrosion inhibitors stands out as one of the most effective and economical methods. Organic inhibitors, especially those containing heteroatoms such as nitrogen (N), sulfur (S), oxygen (O), and phosphorus (P), have demonstrated significant potential in protecting metals from corrosive environments (Dhaef et al., 2019; Di Martino et al., 2022; Temma et al., 2025).

Azo compounds, organic molecules characterized by the presence of the –N=N– azo functional group, are of particular interest due to their structural versatility and potential application as corrosion inhibitors because of the π bond and unpaired electrons in nitrogen atoms, which link onto the metal surface and hinder active sites on the surface, and therewith reduce the corrosion onset (Fouda et al., 2017; Guerra et al., 2018; Ali et al., 2018; Khaled et al., 2021).

Despite ongoing research, a deeper understanding of the relationship between the molecular properties of these compounds and their inhibitory efficiency remains a need. Specifically, few studies have thoroughly correlated quantum chemical parameters with the corrosion inhibition performance of azo dyes in acidic media.

In this study, we aim to investigate the effectiveness of two synthesized azo dyes as corrosion inhibitors for carbon steel in 1 M HCl solution. By employing quantum chemical calculations-namely, E_{HOMO}, E_{LUMO}, energy gap (ΔE), electronegativity (χ), global hardness (η), and the fraction of electron transfer (ΔN)-we seek to clarify the relationship between electronic structure and inhibitory performance. This combined experimental and computational approach enhances our understanding of how molecular properties influence corrosion inhibition efficiency.

This work contributes to the design of azo molecules with unique properties that enhance the inhibition process, as evidenced by the presence of groups that strengthen the bond between the molecules and the metal surface, thereby increasing inhibition. In addition, it combines quantum chemical modeling with real-life corrosion data to predict and elucidate how new azo dyes will perform. This approach not only contributes to the development of more effective inhibitors but also offers a theoretical framework for designing future corrosion-resistant materials.

2. EXPERIMENTAL SECTION

2.1 Materials
Chemicals and solvents were acquired from Sigma-Aldrich (USA). Use TLC plates that are already coated with silica gel 60 and can detect UV light at 254 nm to check how the reaction is going for all the substances made. The IR spectrophotometer (Shimadzu FT-IR Affinity-1, Germany) is used to get FTIR spectra using KBr (1%) discs, which measure from 4000 to 600 cm^{-1}. ^{1}H NMR and ^{13}C NMR readings were taken using a Bruker Inovo AV-400 spectrometer (Iran), with DMSO-d$_6$ as the testing liquid. Chemical shifts (δ scale) were recorded in ppm, and the coupling constant (J) values were identified in Hz. The short forms (s for singlet, d for doublet, t for triplet, and m for multiplet) are used to show how the signals split. The melting point of the compound is measured with a capillary tube using a Gallenkamp device. The precise mass measurements of the compounds created were taken using a JEOL JMS-5X 10217 EI-type instrument (Iran).

2.2 Metal Coupons Composition and Medium
Assessments were conducted on carbon steel (CS) that was composed as described: 0.05% P, 1.2% Mn, 0.3% C, and 0.06% S, with the remaining elements being iron. Using distilled water, HCl was diluted to 1 M concentration (BDH grade, 37%).

2.3 Methods
2.3.1 General Procedure of Synthesis of the Azo Compounds I and II
A 1.265 g, 5 mmol solution of sulfamethoxazole was prepared by dissolving it in a solution of HCl, which was created by mixing equal amounts of concentrated HCl and water. Cooling the solution below 5°C was achieved with an ice bath. A solution of NaNO$_2$ was prepared by dissolving 0.38 g in 10 mL of water, then adding it dropwise to the above solution. An ice bath was used to maintain temperature; hence, the mixture was stirred. Additionally, 0.901 g (5 mmol) of 3-tert-butylhydroxyanisole was added slowly, and the solution was kept at a cool temperature in an ice bath while stirring for an additional 30 minutes. The residue was filtered, followed by recrystallization using an ethanol-based solution. An oven at 50°C was used to dry the necessary solution for 24 hours to produce compound I. The same method was used to prepare compound II, but 2-naphthol was used in the synthesis instead of 3-tert-butylhydroxyanisole.

2.3.2 (E)-4-((3-(Tert-Butyl)-2-Hydroxy-5-Methoxyphenyl) Diazenyl)-N-(5-Methylisoxazol-3-yl)Benzenesulfonamide (I)
A dark orange solid, a yielding 85% purity, m.p. of 200–202°C. IR (ν, cm^{-1}): 3439 cm^{-1} (O–H) phenolic, 3082 C–H aromatic, 2845–2908 C–H aliphatic, 1467 cm^{-1} (N=N), and 1616 cm^{-1} (aromatic C=C). ^{1}H NMR (500 MHz, DMSO) δ (ppm): 1.46 (s, 9H, t-But), 2.31 (s, 3H, CH$_3$), 3.76 (s, 3H, OCH$_3$), 11.2 (s, 1H, NH), 11.57 (s, OH, 1H), 6.19 (s, 1H, isoxazole ring), 7–8.27 (m, 6H, Ar–H). ^{13}C NMR (DMSO-d$_6$) δ/ppm: 12.41, 29.56, 55.80, 96.38, 108.57, 114.96, 123.71, 128.54, 139.11, 140.05, 140.34, 152.12, 153.49, 160.50, 163.50, 174.50. MS [EI]$^+$ m/z 444.3 [M]$^+$.
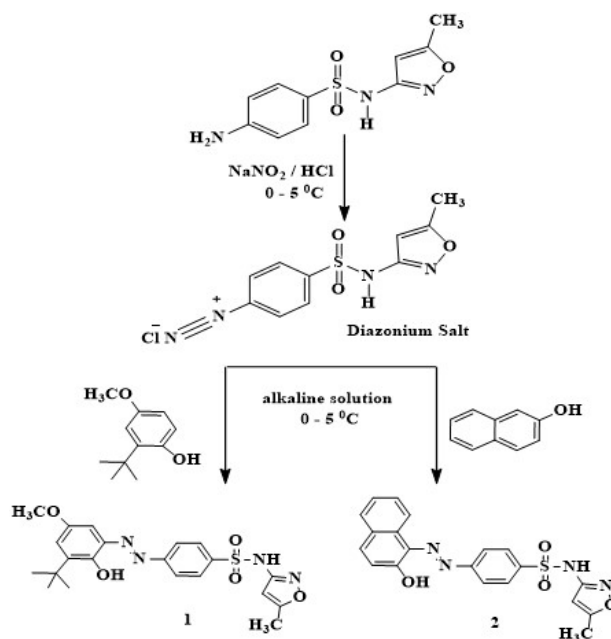

Figure 1. Synthesis Route of Azo compounds I and II

2.3.3 (Z)-4-((2-Hydroxynaphthalen-1-yl)Diazenyl)-N- (5-Methylisoxazol-3-yl)Benzenesulfonamide (II)
A blood-red solid, yielding 88%, m.p. 228–230°C. IR (ν, cm^{-1}): 3441 cm^{-1} (O–H) phenolic, 3064 C–H aromatic, 2831–2987 C–H aliphatic, 1467 cm^{-1} (N=N), 1618 cm^{-1} (aromatic C=C). ^{1}H NMR (500 MHz, DMSO) δ (ppm): 2.31 (s, 3H, CH$_3$), 6.2 (s, 1H, isoxazole ring), 7.34–8.3 (m, 11H, Ar–H), 11.48 (s, 1H, NH), 15.65 (s, OH, 1H). ^{13}C NMR (DMSO-d$_6$) δ/ppm: 12.10, 95.51, 117.53, 121.92, 125.72, 127.08, 128.16, 129.19, 129.54, 129.54, 130.47, 132.58, 135.62, 142.75, 146.56, 157.58, 170.43, 177.42. MS [EI]$^+$ m/z 408.2 [M]$^+$.

2.4 Computational Details
The Gaussian 16, Revision A.03 package program was used for all computations (Frisch et al., 2009), and GaussView 6.0.16 software was used to visualize the results (Dennington et al.,
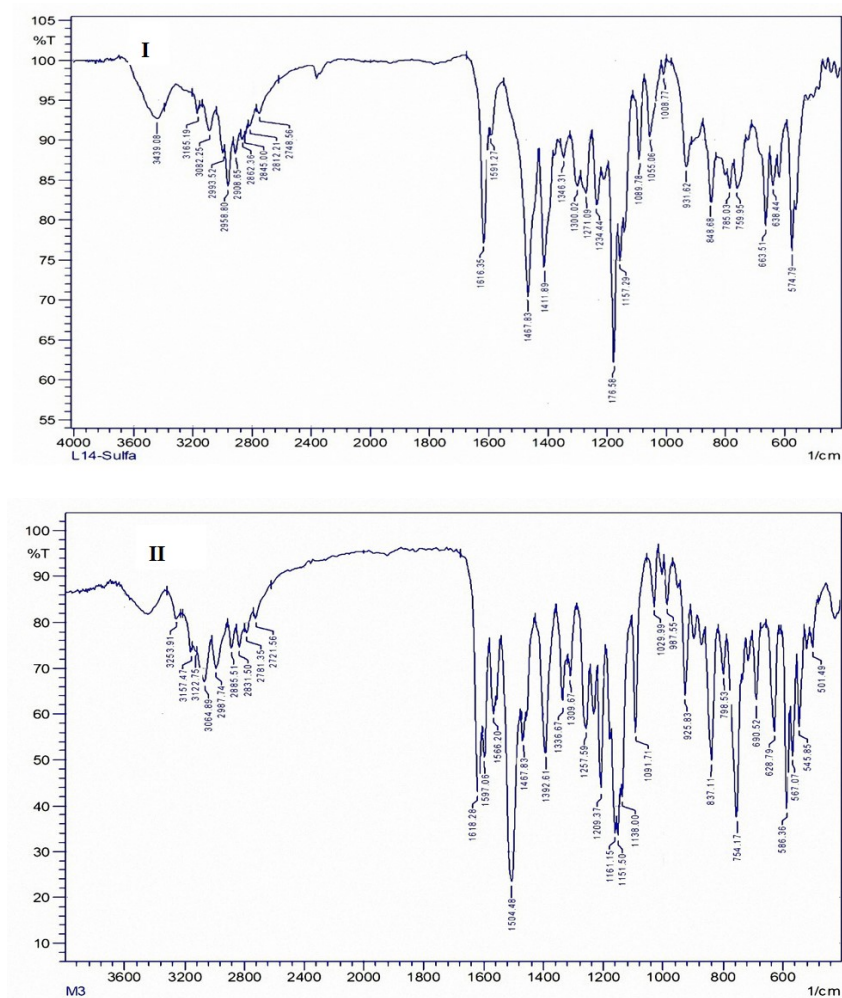
Figure 2. IR Spectra of Compounds I and II

Table 1. Corrosion Parameters for the Galvanostatic Polarization Method of Carbon Steel Corrosion in 1 M HCl in the Presence of Inhibitors I and II

Compound	Concentration of Inhibitor (M)	I_{corr} (mA/cm^2)	E_{corr} (mV)	β_c (mV/Dec)	β_a (mV/Dec)	Θ	IE%	CR (mpy)
HCl	–	50.02	-499.9	126.3	-131.2	–	–	22.78
I	1×10^{-4}	14.1	-487.1	125.8	-123.3	0.71	71.8	6.42
	5×10^{-4}	12.71	-492.7	112.0	-100.3	0.74	74.58	5.79
	1×10^{-3}	11.63	-490.0	107.2	-93.6	0.76	76.7	5.29
	5×10^{-3}	5.01	-488.8	74.2	-64.8	0.89	89.9	2.28
II	1×10^{-4}	17.73	-502.0	137.8	-109.3	0.64	64.55	8.07
	5×10^{-4}	15.71	-491.7	134.4	-112.9	0.68	68.59	7.15
	1×10^{-3}	13.6	-492.0	122.8	-102.2	0.72	72.81	6.19
	5×10^{-3}	8.49	-494.6	88.3	-71.8	0.83	83.02	3.86

2016). Utilizing the 6-311+G(d,p) basis set and the Becke-3-Lee-Yang-Parr (B3LYP) functional, Density Functional Theory (DFT) was employed to optimize the ground-state molecular structure of the molecules (Becke, 1993; Lee et al., 1988). Concurrently, the vibrational frequencies were calculated to detect the absence of imaginary frequencies and confirm that all stationary points on the potential energy surface matched with actual minima. The GaussSum 3.0 software was utilized to calculate the density of states (DOS) (O'boyle et al., 2008).
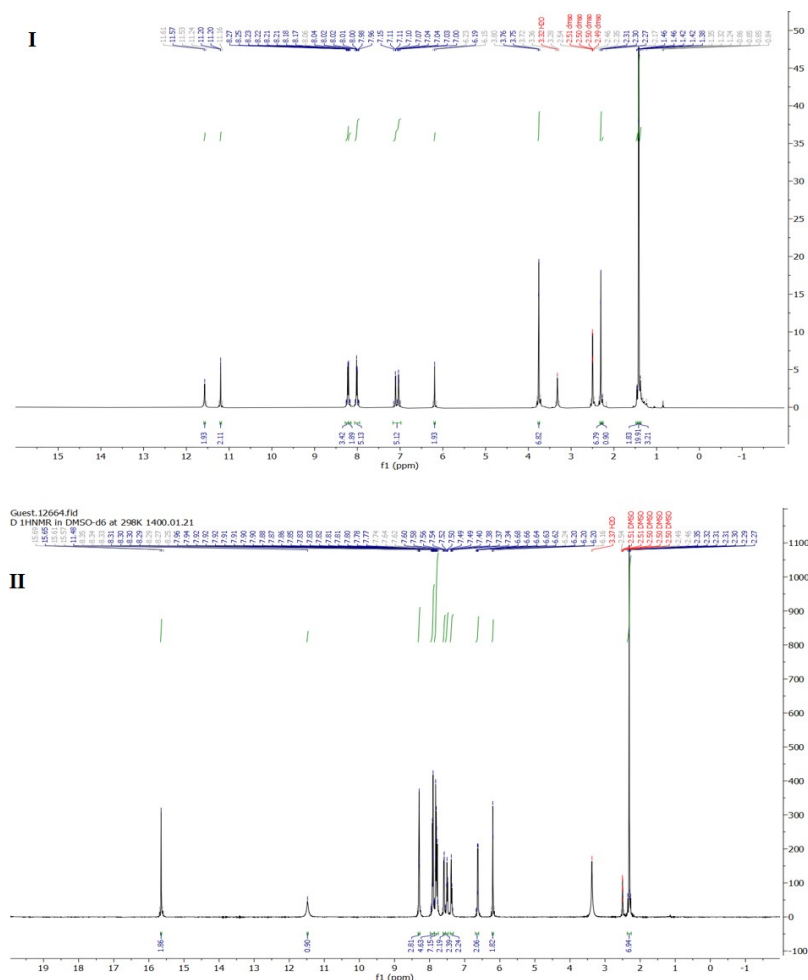
Figure 3. ^{1}H NMR Spectra of Compounds I and II

3. RESULTS AND DISCUSSION

3.1 Chemistry

This study evaluated the use of a diazotization reaction to prepare diazonium salts using sulfamethoxazole, sodium nitrite, and a hydrochloric acid solution. The prepared diazonium chemicals were mixed with 3-tert-butylhydroxyanisole and 2-naphthol to prepare chemicals I and II, as indicated in Scheme 1. Validation of the structures was performed using IR, ^{1}H NMR, ^{13}C NMR, and mass spectrometry (Pavia, 2001).

The compounds were examined using IR spectroscopy, which revealed key absorption peaks at 3439 cm^{-1} for compound I and 3441 cm^{-1} for compound II, indicating the presence of OH groups. Additionally, absorption bands between 3082 and 3064 cm^{-1} were observed, corresponding to C–H$_{aromatic}$ bonds in both compounds. The methyl group's C–H bonds in both compounds also exhibited weak absorption at 2880–2900 cm^{-1}. Furthermore, both compounds exhibit C–H bonds originating from the methyl group. At the same time, the C–H of the methyl group of both compounds showed weak absorption at 288–2900 cm^{-1}. At 1467–1618 cm^{-1}, all syn-

thesized compounds showed absorptions attributed to N=N and C=C$_{aromatic}$, respectively. As shown in Figure 2.

The proton NMR spectra of the made compound I showed singal signal at 1.46 ppm representing 9 protons from three methyl groups in tetrabutyl, singal signal at 2.31 ppm for 3 protons from the methyl group, and singal signal at 3.76 ppm for 3 protons from the methoxy group, which showed a higher shift because of its connection to the oxygen atom. The spectrum also showed a single signal at 6.19 ppm attributed to one proton from the methine group in the isoxazole ring. Multiple signals at shifts 7-8.27 ppm were attributed to the 6 protons of the aromatic ring. Two single signals at shifts 11.24 ppm and 11.61 ppm, with one proton each, were attributed to the amine and hydroxy groups, respectively.

In the same context, the ^{1}H NMR of compound II showed a single peak at 2.31 ppm, representing three protons from the methyl group, and another single peak at 6.2 ppm, originating from the methine group in the isoxazole ring. Multiple peaks were also found between 7.34 and 8.31 ppm, corresponding to 11 protons. Two separate peaks were observed at 11.48 ppm and 15.65 ppm, corresponding to the single protons from the
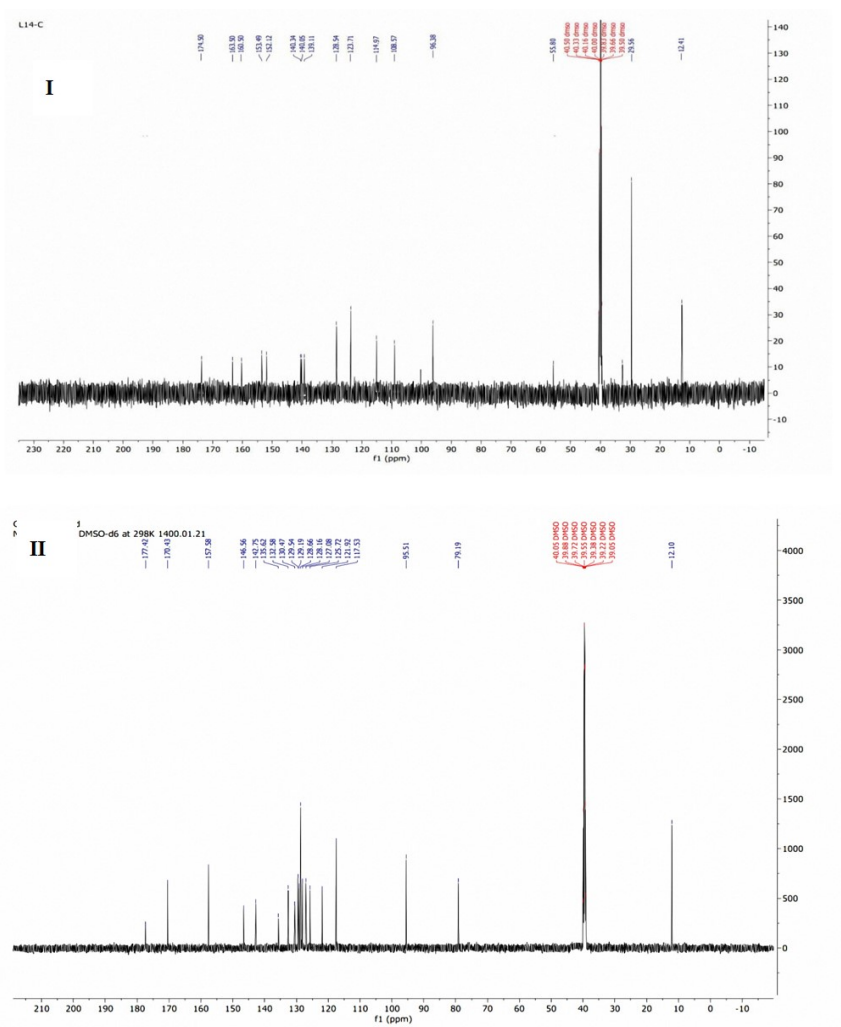
Figure 4. ^{13}C NMR Spectra of Compounds I and II

Table 2. The Adsorption Thermodynamic Parameters of Compounds I and II on the Carbon Steel Surface in 1 M HCl at 298 K

Compound	R^2	$\log K_{\text{ads}}$	$\Delta G^{\circ}_{\text{ads}}$ (kJ mol^{-1})	$\Delta H^{\circ}_{\text{ads}}$ (kJ mol^{-1})	$\Delta S^{\circ}_{\text{ads}}$ (kJ mol^{-1} K^{-1})
I	0.9991	3.937206	-32.4119	-7.94229	0.135417
II	0.9995	3.936819	-32.4097	-10.5091	0.108757

NH and OH groups, respectively, as shown in Figure 3.

The structure of the generated compounds was confirmed by the following indicators from the ^{13}C NMR spectra: The ^{13}C NMR spectrum of compound I showed a peak at 12.41 ppm for the methyl group, 29.56 ppm for the tert-butyl methyl group, 55.80 ppm for the methoxy methyl group, and several peaks between 95.38 and 174.50 ppm for carbon atoms in the aromatic rings and the isoxazole ring. The same applies to compound II's spectrum, which has a signal at 12.10 ppm for the methyl group and several signals between 95.93 and 177.42 ppm for carbon atoms in the aromatic rings and the isoxazole ring. As shown in Figure 4.

Furthermore, the mass spectra of the substances confirm that the peaks of the molecular ions occur at m/z 444.3 and m/z 408.2 for the first and second compounds, respectively. Figure 5 illustrates.

3.2 Potential Dynamic Polarisation Measurements

The electrochemical kinetics of metallic corrosion can be characterized by obtaining a minimum of three polarizing parameters: corrosion current density (I_{corr}), corrosion potential (E_{corr}), and Tafel slopes (β_a and/or β_c). To assess the corrosion behaviour, employ an E vs. $\log I$ polarization curve. The corrosion rate is assessed through the evaluation of polarization
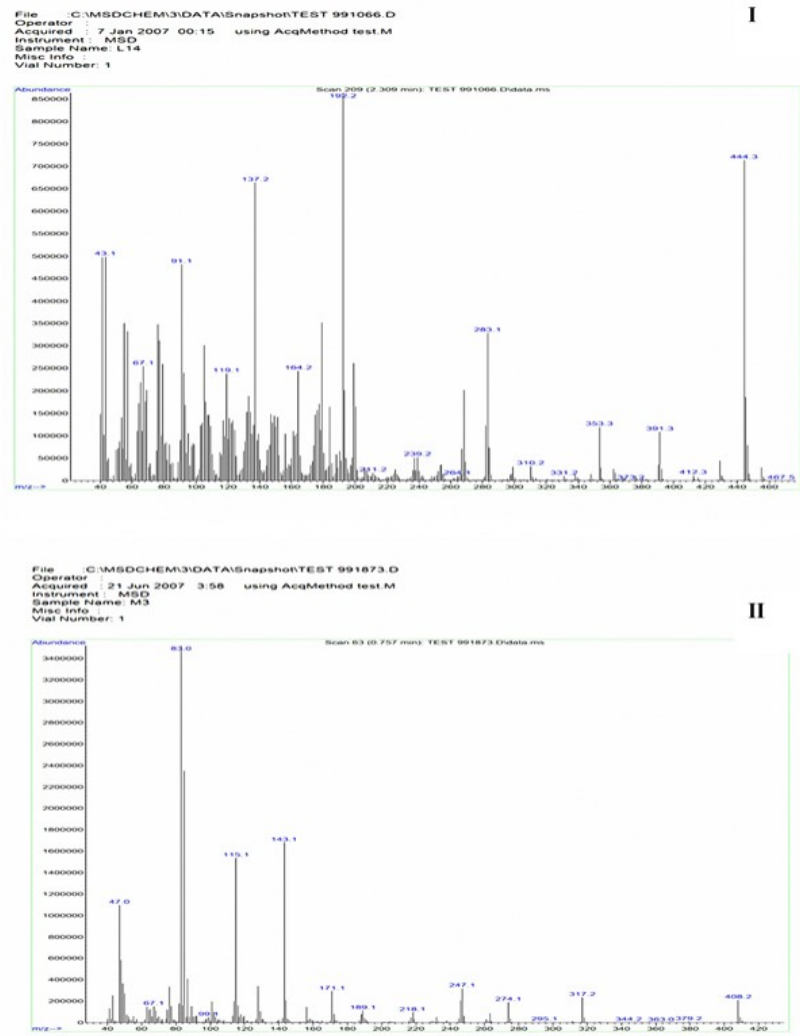
Figure 5. Mass Spectra of Compounds I and II

Table 3. Ground State Properties of the Azo Compounds Using B3LYP/6-311+G(d,p)

Compound	HOMO (eV)	LUMO (eV)	ΔE (eV)	χ (eV)	η (eV)	ΔE (Back Donation)	S (1/η)	ω	ΔN
I	-6.0199	-3.1826	2.8373	4.6012	1.4186	-0.3546	0.7048	7.4619	1.9671
II	-5.9957	-2.7546	3.2411	4.3751	1.6205	-0.4051	0.6170	5.9059	1.6597

characteristics (CR). Consequently, I_{corr} was computed for the blank (a solution lacking an inhibitor) and all concentrations of the evaluated inhibitors, as illustrated in Figure 1. The electrochemical results are shown in Table 1, which includes the corrosion potential (E_{corr}), corrosion current density (I), the slopes for anodic and cathodic reactions, and the efficiency of the inhibitors (IE%) (Abood et al., 2024). Figure 6 illustrates the behavior of carbon steel in 1 M HCl with and without the added inhibitors I and II at 298 K. The results show that the reactions at the anode and cathode, using the carbon steel electrode, had less corrosion when high amounts of inhibitors were used. Therefore, it was established that including inhibitors limited anodic dissolution and hydrogen evolution. Tafel plots helped reveal important electrochemical details, including the anodic Tafel constant (β_a), cathodic Tafel constant (β_c), corrosion rate (CR), corrosion potential (E_{corr}), and corrosion current density (I_{corr}) (Fawzy and Toghan, 2021; Merdan et al., 2019). Table 1 lists the outcomes concerning several electrochemical parameters. The inclusion of corrosion inhibitors limited the current density. The peak reduction in I_{corr} levels was observed for chemicals at a concentration of 5×10^{-3}. When compounds I and II were mixed with 1 M HCl, the E_{corr} levels for these
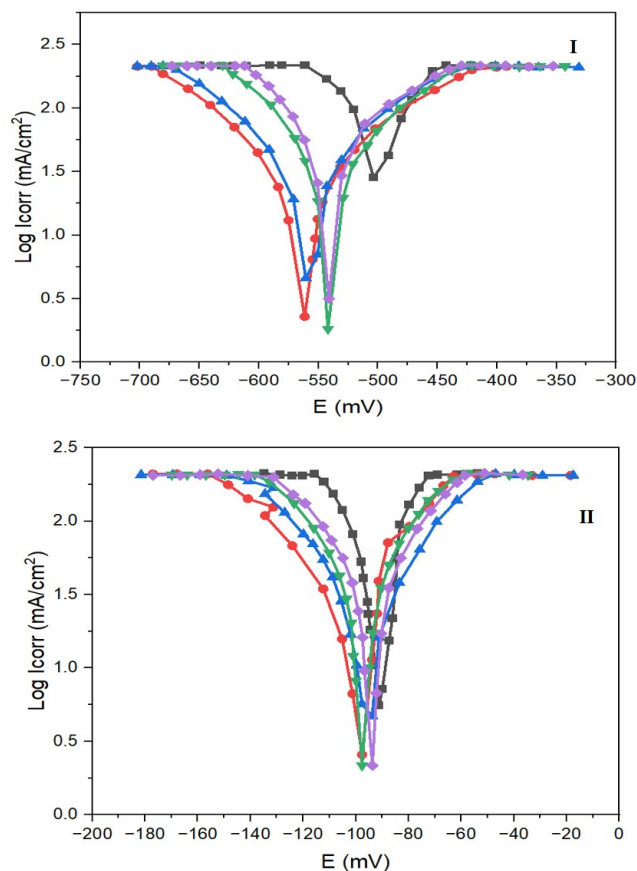
Figure 6. Carbon Steel Corrosion Polarization Curves in 1M HCl, in the Presence and Absence of Compounds I and II at 298 K

chemicals changed a little in both the positive and negative directions, but there was no clear pattern. The findings revealed that the compounds have various inhibitory properties. These substances changed the anodic and cathodic Tafel plots, showing that the inhibitors influenced how much they covered the metal surface, and the inhibition efficiency (IE%) was estimated (2) (Abdulridha et al., 2020): using the previously mentioned two equations, Equations 1 and 2. The results showed that compound I has more inhibition efficiency than compound II.

$$IE\% = \left[\frac{I_{corr} - I_{corr\,(inh)}}{I_{corr}} \right] \times 100 \tag{1}$$

$$\theta = \left[1 - \frac{I_{corr\,(inh)}}{I_{corr}} \right] \tag{2}$$

Where $I_{corr\,(inh)}$ represents the corrosion current in the absence of an inhibitor, while I_{corr} represents the corrosion current in the presence of an inhibitor.
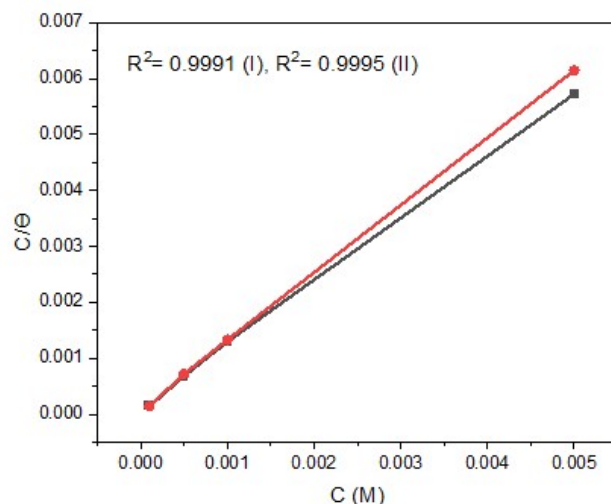

Figure 7. The Langmuir Curve for Carbon Steel Corrosion at 298 K is Shown for the Researched Compounds I and II in a 1 M HCl Solution

3.3 Adsorption Isotherm

Most relevant studies employ adsorption thermodynamics methods to explain how corrosion inhibitors adsorb or interact with metals. The computed thermodynamic parameters of adsorption are crucial for analyzing the mechanism of the adsorption process on a metal surface. The way an inhibitor attaches to a metal surface, whether through physisorption, chemisorption, or a combination of both, can typically be identified by examining factors such as the adsorption equilibrium constant (K_{ads}), adsorption free energy (ΔG_{ads}), enthalpy (ΔH_{ads}), and entropy (ΔS_{ads}).
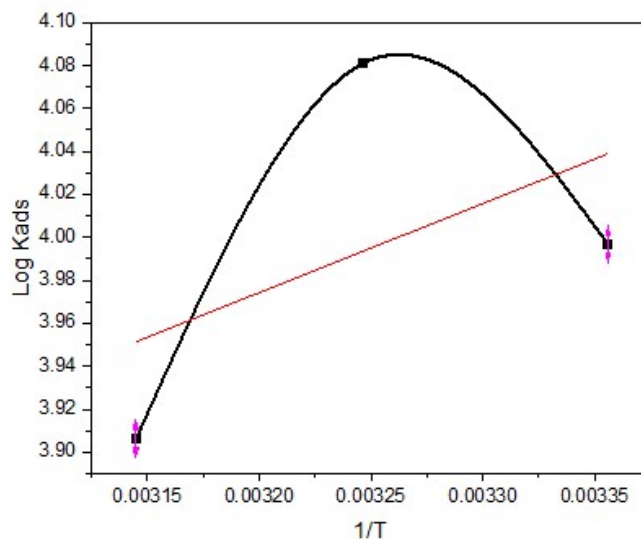

Figure 8. Log Kads and 1/T in a Solution of 1 M HCl at 298 K for Carbon Steel Compound I
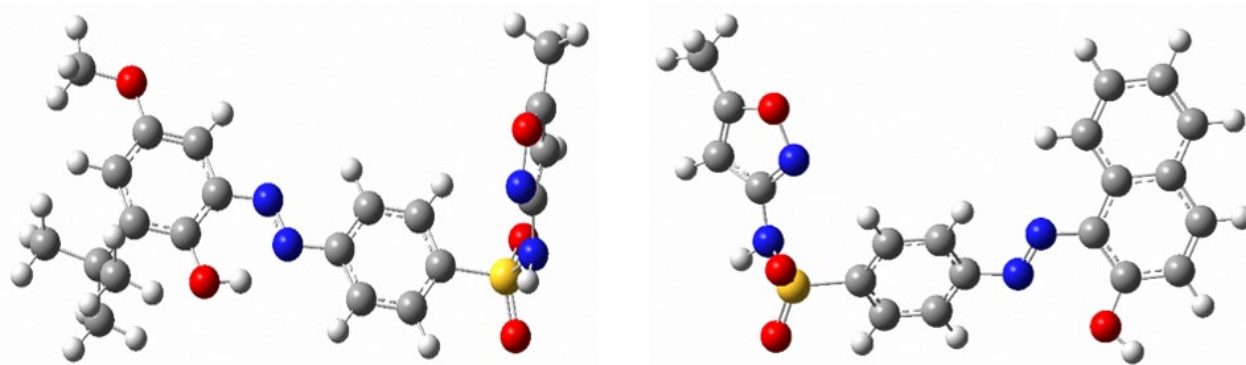
Figure 9. Geometry Optimization of Compounds I and II

According to data from the organic molecule's adsorption, interactions between the surface of the electrode and the molecules take place. The two main categories regarding organic molecular adsorption are physical and chemical adsorption. The type of electrolyte influences adsorption and the arrangement of the inhibitor chemical, as well as the nature and properties of the metal. Equation 2 has been used to calculate, employing a 1 M HCl solution, the degree of surface coverage (θ) for numerous inhibiting reagent doses. Additionally, Table 1 shows values for θ.

In this context, the current density values of corrosion are denoted by the symbols I_{corr} and I_{corr}°, which refer respectively to the inhibited and uninhibited cases. It has been observed that Equation 3 and the score agree because the Langmuir isotherm is described via the comprehensive term (Rao et al., 2019).

$$\frac{C}{\theta} = \frac{1}{K_{\text{ads}}} + C \qquad (3)$$

Here, C represents the inhibitor concentration (M), θ indicates the surface coverage, while K_{ads} determines a steady state relating to the adsorptive balance. To determine an appropriate straight-line correlation, surface coverage (θ) was obtained graphically. As shown in Table 2, the determinative coefficient (R^2) values were 0.9991 and 0.9995. As introduced in Figure 7, the outcomes demonstrate how the Langmuir adsorption isotherm can be employed to accurately portray the characteristics of inhibiting adsorption with a satisfactory level of accuracy. The excellent correlation with the Langmuir adsorption isotherm validates this method. The equilibrium constant (K_{ads}), which is consistent with the adsorption phenomena, has been determined using the value of the intercept in reciprocal mode. Table 2 shows the fixed values of equilibrium. The substantial magnitudes imply that the selected inhibitor has acceptable carbon steel surface adsorption capability. These results can be explained by the establishment of concerted ties between the produced chemical and the d-orbitals of the iron molecules on the steel's surface.

3.4 Thermodynamic Parameters

The adsorption free energy (ΔG_{ads}), enthalpy (ΔH_{ads}), and entropy (ΔS_{ads}) can be ascertained using K_{ads} values derived from the optimal adsorption isotherm fit. The formulas for calculating all the specified parameters are presented in Equation 4 (Fawzy and Toghan, 2021):

$$\Delta G_{\text{ads}}^{\circ} = -RT \ln\left(55.5\, K_{\text{ads}}\right) \qquad (4)$$

The amount of water expressed by M is 55.5 in a solution. R stands for the gas constant (8.314 J mol^{-1} K^{-1}), and T is the absolute temperature. As a function of $\Delta G_{\text{ads}}^{\circ}$ regarding inhibitor molecules, spontaneous adsorption is expressed by a negative value over the surface of the steel. These values are typically specified for physisorption, which occurs when charged inhibitor molecules interact electrostatically with the surface of a charged metal, with $\Delta G_{\text{ads}}^{\circ} \approx -20$ kJ mol^{-1}. However, chemisorption occurs with a $\Delta G_{\text{ads}}^{\circ} > -40$ kJ mol^{-1} as a result of the electrons' transmission or participation between the inhibitor molecule and the metal's corresponding orbitals, resulting in a harmonious bond (Alfakeer et al., 2020). In this research, the derived $\Delta G_{\text{ads}}^{\circ}$ magnitudes were used to indicate chemisorption (mixed adsorption). In a mixture of chemisorption and physisorption processes in a 1 M HCl solution, azo compounds were observed to induce an adsorption mechanism on carbon steel (Abdulridha et al., 2020). Adsorption heat is calculated by using the Van't Hoff Equation 5 (Negm et al., 2010):

$$\log K_{\text{ads}} = \frac{-\Delta H_{\text{ads}}}{2.303\, RT} + \text{Const} \qquad (5)$$

Here, the adsorption heat constant is denoted by $\Delta H_{\text{ads}}^{\circ}$, and K_{ads} stands for the constant of adsorptive equilibrium. Here, losing versus $1/T$ results in a gain of the basic steady climax at 311.2 in Figure 8, which allows for providing a straight-line reference to Equation 5, where the slope $= -\Delta H_{\text{ads}}^{\circ}/R$. The negative $\Delta H_{\text{ads}}^{\circ}$ magnitudes indicate the exothermic adsorption of the examined chemicals on the carbon steel surface. Em-
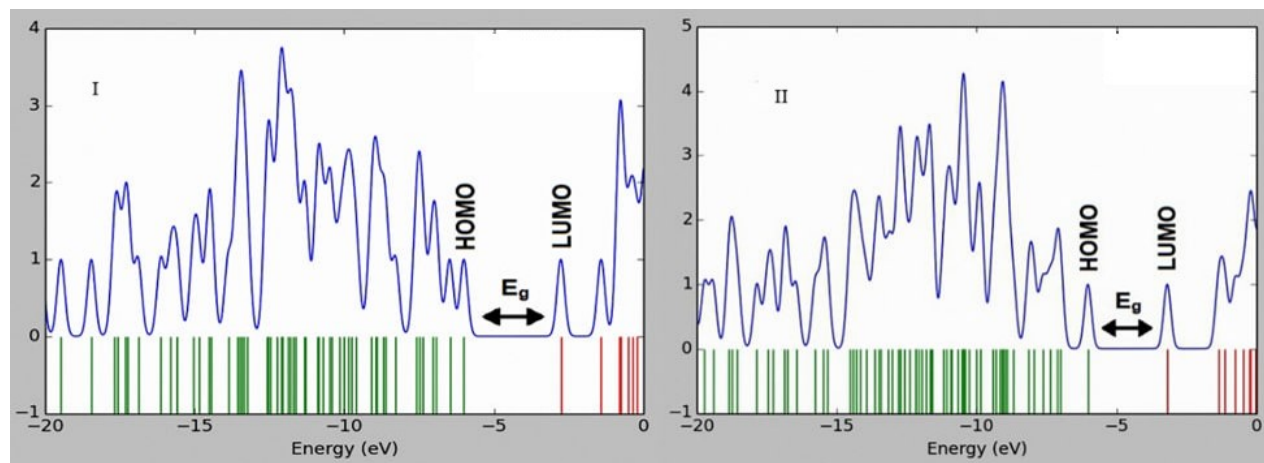
Figure 10. Molecular Orbital Surfaces for the HOMO–LUMO of Azo Compounds I and II

ploying Equation 6, the entropy of inhibitor adsorption ΔS°_{ads} is determined (Alfakeer et al., 2020).

$$\Delta G^\circ_{ads} = \Delta H^\circ_{ads} - T \Delta S^\circ_{ads} \qquad (6)$$

The calculated magnitudes of S°_{ads} are shown in Table 2. Entropy increases with positive S°_{ads} values during the adsorption process, which is anticipated due to entropy augmentation as it tracks endothermic adsorption, describing the driving force for inhibitor adsorption onto the surface of carbon steel (Tawfik et al., 2012).

3.5 DFT Study

The Gaussian 09W software package was employed for DFT calculations using a hybrid functional (B3LYP) at the 6-311G+ (d,p) basis set (Feng et al., 2018). Quantum chemical techniques are helpful for elucidating electronic structure, reactivity, and molecular structure. In the current study, the relationship between molecular structures was evaluated by quantum chemical calculations, as well as the inhibition impact on the brass surface via DFT studies. The HOMO, LUMO, χ, η, S, ω, and ΔE for the Azo-compounds are shown in Figure 9 and Table 3.

The quantum chemical factors are shown in Table 3. The HOMO and LUMO energies determine the donor and acceptor abilities of the inhibitor molecule in the inhibitor/metal surface interaction, according to the FMO hypothesis (Gouda et al., 2022). A molecule's ability to donate is termed E_{HOMO}, and its ability to accept is termed E_{LUMO}. As a result, a molecule with a large E_{HOMO} value acts as an inhibitor, supplying the metal's vacant orbital with electrons. A molecule with an E_{LUMO} value indicates the ability to receive electrons via reverse donation from the metal orbital (Abd El-Lateef et al., 2020). Table 3 shows that when compared to I and II, the E_{HOMO} and E_{LUMO} values of II are the highest at -5.9957 and -2.7546 eV, respectively. The molecular electrical transport properties have been investigated based on the HOMO-LUMO energy gap (ΔE), as it demonstrates the ultimate transfer of charge interaction within the molecule (Miar et al., 2021). Molecules with high HOMO-LUMO energy gaps demonstrate low chemical reactivity and high kinetic energy (Aihara, 1999; Madkour and Elroby, 2015). Because only a small amount of ionization energy is required to remove an electron from the orbital that has been most recently occupied, a low E value can be considered a characteristic of an efficient corrosion inhibitor (Erdogan et al., 2017). A small ΔE for I (2.8373 eV) indicates high chemical reactivity, low kinetic stability, and good corrosion inhibition compared with II (3.2411 eV), because electron migration from HOMO to LUMO is energetically favorable (Ozdemir et al., 2022; Seth et al., 2011). The other important characteristic is electronegativity (χ). It is a property that measures an atom's ability or set of atoms to withdraw electrons, which might be determined from $\chi = -\frac{1}{2}(E_{HOMO} + E_{LUMO})$ (Xavier et al., 2015). The electrons in the inhibitor are concentrated more locally compared to those in other compounds because they have a high electronegativity value. Inhibitors interact with the appropriate molecules of acceptors by donating electrons. Thus, inhibition efficiency rises as the electronegativity value rises (Sayin and Jafari, 2016). The following pattern exists for the inhibition efficiency of the compounds being assessed: I > II.

Chemical hardness (η) is an indicator of resistance to switching electron distribution or charge transfer; it is defined in the formula $\eta = 0.5(E_{LUMO} - E_{HOMO})$ (Slodek et al., 2021). It is anticipated that the anticorrosive inhibitors will be the molecules that possess the lowest global hardness values for bulk metals in acidic conditions. In our study, the following order of anticorrosion efficiency has been estimated: I > II. Also, $\Delta E_{back-donation} = -\frac{\eta}{4}$ was employed to determine the energy of back donation ($\Delta E_{back-donation}$) (Gómez et al., 2006; Guo et al., 2018). So, as per the previous formula, when $\eta > 0$ or $\Delta E_{back-donation} < 0$, it is believed that the back-donations from molecules to metal are more energetic, making them energetically desirable, i.e., the transfer of charge to a molecule

as well as subsequent back-donations from the molecule. With regards to the data presented in Table 3, the following order is associated with the estimated $\Delta E_{\text{back-donation}}$ values, which is expected as well as compatible with the empirical observations I > II.

The inverse of hardness is softness. It is given by the formula $S = \frac{1}{\eta}$ (Kaya et al., 2016). Softness is an indicator of polarizability because soft chemicals donate electrons to surfaces or electron acceptor chemicals more readily (Kannan et al., 2016). Molecules with a small energy gap are smooth, and the softness of these molecules increases their inhibition efficiency (Allal et al., 2018). According to Table 3, the I molecule has a lower E energy and a higher softness value than the II molecule, indicating that it may have a more substantial inhibitive impact on the steel surface as a corrosion prevention.

The quantity of electrophilicity (ω) is a valuable quantum chemical property for predicting the chemical behaviour of molecules, which can be utilized to evaluate the efficiency of inhibiting chemicals. It is defined as a measure of a molecule's capacity to accept and/or donate electrons; a low value of the index indicates an excellent nucleophile (donor), whereas a high value indicates an excellent electrophile (acceptor), and can be determined as $\omega = \chi^2/2\eta$ (Obot and Obi-Egbedi, 2010). According to values in Table 3, the electrophilicity of II is less than that of I. The corrosion inhibition efficiency of the examined compounds can then be sorted as follows: II > I. This result is inconsistent with practical outcomes.

The fraction of transferred electrons (ΔN_{max}): The number of electrons that were accepted by the metallic atom from the inhibitor molecule (ΔN_{max}) was estimated by the formula $\Delta N_{\text{max}} = (\chi_{\text{Fe}} - \chi_{\text{inh}})/2(\eta_{\text{Fe}} + \eta_{\text{inh}})$, where χ_{Fe} displays the electronegativities of Fe metal and equals 7 eV. η_{Fe} represents a hardness of Fe = 0, χ_{inh}, and η_{inh} represent the electronegativities and chemical hardness of the inhibitor, respectively. Inhibition efficiency is increased by low hardness and high electron transfer efficiency. Based on the results in Table 3, I have greater inhibitory effects than II. This finding is consistent with the experimental study by Obot and Obi-Egbedi (2010).

3.6 Density of States (DOS) of Compounds

Figure 10 illustrates the density of states spectrum for compounds I and II. The organization's contributions to the LUMO and HOMO molecular orbitals have been observed using it. The number of orbitals visible at the given energy level was displayed on the DOS graph (Rouhani, 2019). A reduction in the band gap is associated with an increase in conductivity, as the band gap energy, E_g, primarily determines electrical conductivity. The relationship between conductivity and E_g can be clarified using Equation 7.

$$\sigma \propto \exp\left(\frac{E_g}{kT}\right) \qquad (7)$$

Wherein k is the Boltzmann constant and σ is the electrical conductivity. As shown in this, a rise in electrical conductivity

is enhanced by a reduction in the band gap E_g (Ismael et al., 2024). Compared to II, I exhibit a greater ability for electrical conductivity, as indicated by the ΔE values in Table 3.

4. CONCLUSIONS

The synthesized azo compounds can be used as corrosion inhibitors. Both compounds (I and II) have exhibited inhibition efficiencies of 89.9% and 83.02%, respectively, at a concentration of 5×10^{-3} M. The results indicate that synthetic compound I is highly effective in preventing corrosion, as its ability to inhibit it increases with increasing concentration. Density functional theory, using the B3LYP method and detailed calculations, was employed to investigate the electronic structures and properties that influence the effectiveness of the compounds in preventing corrosion. These characteristics were found to be crucial for interpreting molecular effectiveness and inhibition efficiency. Moreover, the experimental and theoretical data displayed a good agreement. Therefore, these compounds can be developed to be more suitable for use against corrosion.

5. ACKNOWLEDGEMENT

REFERENCES

Abd El-Lateef, H. M., K. Shalabi, and A. H. Tantawy (2020). Corrosion Inhibition of Carbon Steel in Hydrochloric Acid Solution Using Newly Synthesized Urea-Based Cationic Fluorosurfactants: Experimental and Computational Investigations. *New Journal of Chemistry*, **44**(41); 17791–17814

Abdulridha, A. A., M. A. A. H. Allah, S. Q. Makki, Y. Sert, H. E. Salman, and A. A. Balakit (2020). Corrosion Inhibition of Carbon Steel in 1 M H_2SO_4 Using New Azo Schiff Compound: Electrochemical, Gravimetric, Adsorption, Surface and DFT Studies. *Journal of Molecular Liquids*, **315**; 113690

Abood, H. S., E. Q. Jasim, and M. A. Muhammad-Ali (2024). Synthesis, Corrosion Inhibition Efficiency in Acidic Media, and Quantum Chemical Studies of Some Hydrazine Derivatives. *Science and Technology Indonesia*, **9**(1); 137–147

Aihara, J. (1999). Reduced HOMO–LUMO Gap as an Index of Kinetic Stability for Polycyclic Aromatic Hydrocarbons. *The Journal of Physical Chemistry A*, **103**(37); 7487–7495

Al-Hujaj, H. H., F. A. Almashal, A. T. Kadum, M. K. Mohammed, K. A. Hussein, and A. M. Jassem (2023). Click Chemistry-Based Synthesis of Novel 1,2,3-Triazole Derivatives and Cytotoxic Activity on Breast and Prostate Cancer Cell Lines. *Tropical Journal of Natural Product Research*, **7**(7); 3306–3313

Alfakeer, M., M. Abdallah, and A. Fawzy (2020). Corrosion Inhibition Effect of Expired Ampicillin and Flucloxacillin

Drugs for Mild Steel in Aqueous Acidic Medium. *International Journal Electrochemical Science*, **15**; 3283–3297

Allal, H., Y. Belhocine, and E. Zouaoui (2018). Computational Study of Some Thiophene Derivatives as Aluminium Corrosion Inhibitors. *Journal of Molecular Liquids*, **265**; 668–678

Ashoor, M. J., S. M. H. Ismael, H. M. Jarallah, H. A. Sultan, Q. M. A. Hassan, K. A. Hussein, and C. A. Emshary (2025). Nonlinear Optical Properties of Azo Compound Synthesized Via Diazonation Reaction Using Continuous Wave Laser Beams. *Applied Physics B*, **131**(4); 71

Becke, A. D. (1993). Density-Functional Thermochemistry. III. The Role of Exact Exchange. *The Journal of Chemical Physics*, **98**(7); 5648–5652

Dennington, R., T. A. Keith, and J. M. Millam (2016). Environmentally Friendly Room Temperature Synthesis of 1-Tetralone over Layered Double Hydroxide-Hosted Sulphonato-Salen-Nickel(II) Complex. *Semichem Inc Shawnee Mission KS*, **13**(1); 9–22

Dhaef, H. K., E. Q. Jasim, Z. A. Muhajjar, and A. A. Shanta (2019). Corrosion Inhibition of Mild-Steel in 0.5 M HCl Using Some Prepared 1,2,3-Triazoles Derivatives. *Mediterranean Journal of Chemistry*, **2019**(4); 290–304

Dhaif, H. K., E. Q. Jasim, H. A. A. Rafid, and K. M. Mohammed (2022). Synthesis, Corrosion Inhibition Study and DFT Calculation of Two New Azo Compounds. *Egyptian Journal of Chemistry*, **65**(12); 481–492

Di Martino, M., L. Sessa, M. Di Matteo, B. Panunzi, S. Piotto, and S. Concilio (2022). Azobenzene as Antimicrobial Molecules. *Molecules*, **27**(17); 5643

Erdogan, S., Z. S. Safi, S. Kaya, D. O. Işın, L. Guo, and C. Kaya (2017). A Computational Study on Corrosion Inhibition Performances of Novel Quinoline Derivatives Against the Corrosion of Iron. *Journal of Molecular Structure*, **1134**; 751–761

Fawzy, A. and A. Toghan (2021). Inhibition Evaluation of Chromotrope Dyes for the Corrosion of Mild Steel in an Acidic Environment: Thermodynamic and Kinetic Aspects. *ACS Omega*, **6**(5); 4051–4061

Feng, L., C. Yin, H. Zhang, Y. Li, X. Song, Q. Chen, and H. Liu (2018). Cationic Gemini Surfactants With a Bipyridyl Spacer as Corrosion Inhibitors for Carbon Steel. *ACS Omega*, **3**(12); 18990–18999

Frisch, M. J., G. W. Trucks, H. B. Schlegel, G. E. Scuseria, M. A. Robb, J. R. Cheeseman, G. Scalmani, V. Barone, B. Mennucci, G. A. Petersson, et al. (2009). Gaussian 09. Wallingford CT

Gouda, M., M. M. Khalaf, K. Shalabi, M. A. Al-Omair, and H. M. A. El-Lateef (2022). Synthesis and Characterization of Zn–Organic Frameworks Containing Chitosan as a Low-Cost Inhibitor for Sulfuric-Acid-Induced Steel Corrosion: Practical and Computational Exploration. *Polymers*, **14**(2); 228

Guo, L., Z. S. Safi, S. Kaya, W. Shi, B. Tüzün, N. Altunay, and C. Kaya (2018). Anticorrosive Effects of Some Thiophene Derivatives Against Iron Corrosion: A Computational Study.

Frontiers in Chemistry, **6**; 155

Gómez, B., N. V. Likhanova, M. A. Domínguez-Aguilar, R. Martínez-Palou, A. Vela, and J. L. Gázquez (2006). Quantum Chemical Study of the Inhibitory Properties of 2-Pyridyl-Azoles. *Journal of Physical Chemistry B*, **110**(18); 8928–8934

Ismael, S. M. H., N. S. Hashim, F. A. Al-Saymari, H. A. Sultan, Q. M. A. Hassan, K. A. Hussein, C. A. Emshary, and H. M. Jarallah (2024). Synthesis of an Azo Compound: Investigation of its Optical Nonlinear Properties and DFT Study. *Journal of Fluorescence*, **35**; 7241–7260

Jarallah, H. M. and S. H. Ali (2025). Synthesis, Characterization, Thermal Analysis, DFT, and Computational/Anti-Corrosion Studies for New Azo Metal Complexes. *Indonesian Journal of Chemistry*, **25**(2); 534–547

Kannan, P., J. Karthikeyan, P. Murugan, T. S. Rao, and N. Rajendran (2016). Corrosion Inhibition Effect of a Novel Methylbenzimidazolium Ionic Liquid on Carbon Steel in HCl Medium. *Journal of Molecular Liquids*, **221**; 368–380

Kaya, S., C. Kaya, L. Guo, F. Kandemirli, B. Tüzün, I. Uğurlu, L. H. Madkour, and M. Saraçoğlu (2016). Quantum Chemical and Molecular Dynamics Simulation Studies on the Inhibition Performances of Some Thiazole and Thiadiazole Derivatives Against the Corrosion of Iron. *Journal of Molecular Liquids*, **219**; 497–504

Lee, C., W. Yang, and R. G. Parr (1988). Development of the Colle-Salvetti Correlation-Energy Formula into a Functional of the Electron Density. *Physical Review B*, **37**(2); 785

Madkour, L. H. and S. K. Elroby (2015). Inhibitive Properties, Thermodynamic, Kinetics and Quantum Chemical Calculations of Polydentate Schiff Base Compounds as Corrosion Inhibitors for Iron in Acidic and Alkaline Media. *International Journal of Industrial Chemistry*, **6**(3); 165–184

Merdan, M., D. J. A. D. F. Al-Den, Y. Al-Khafaji, and A. S. Abbas (2019). Theoretical Study for Chromen Azodye Derivative Compounds as Anti-Corrosive. *Journal of Physics: Conference Series*, **1234**(1); 012054

Miar, M., A. Shiroudi, K. Pourshamsian, A. R. Oliaey, and F. Hatamjafari (2021). Theoretical Investigations on the HOMO–LUMO Gap and Global Reactivity Descriptor Studies, Natural Bond Orbital, and Nucleus-Independent Chemical Shifts Analyses of *3-phenylbenzo[d]thiazole-2(3H)-imine* and its Para-Substituted Derivatives: Solvent and Substituent Effects. *Journal of Chemical Research*, **45**(1-2); 147–158

Negm, N. A., Y. M. Elkholy, M. K. Zahran, and S. M. Tawfik (2010). Corrosion Inhibition Efficiency and Surface Activity of Benzothiazol-3-Ium Cationic Schiff Base Derivatives in Hydrochloric Acid. *Corrosion Science*, **52**(10); 3523–3536

Obot, I. B. and N. O. Obi-Egbedi (2010). Theoretical Study of Benzimidazole and its Derivatives and Their Potential Activity as Corrosion Inhibitors. *Corrosion Science*, **52**(2); 657–660

Ozdemir, N., M. Kaloğlu, N. Kaloğlu, N. Gürbüz, and

I. Ozdemir (2022). Synthesis, Characterization, Crystal Structure, Hirshfeld Surface Analysis, and Theoretical Study on a N-Heterocyclic Carbene Salt and Two NHC–Palladium Complexes. *Inorganic and Nano-Metal Chemistry*, **52**(4); 493–504

O'boyle, N. M., A. L. Tenderholt, and K. M. Langner (2008). Cclib: a Library for Package-Independent Computational Chemistry Algorithms. *Journal of Computational Chemistry*, **29**(5); 839–845

Pavia, L. G. K. G. V. J., D.L. (2001). *Introduction to Spectroscopy*, 3rd ed., Thomson Learning Inc.

Rao, Y., P. K. P, D. Sunil, P. Shetty, and S. A. Rao (2019). Attenuation of Acid Corrosion of Mild Steel Using a Novel Organic Dye: Electrochemical and Surface Measurements. *Protection of Metals and Physical Chemistry of Surfaces*, **55**(4); 443–454

Rouhani, M. (2019). A Detailed Computational Investigation on the Structural and Spectroscopic Properties of *propolis-benzofuran* B. *Heliyon*, **5**(10); e02518

Sayin, K. and H. Jafari (2016). Effect of Pyridyl on Adsorption Behavior and Corrosion Inhibition of Aminotriazole. *Journal of the Taiwan Institute of Chemical Engineers*, **68**; 431–439

Seth, S. K., N. C. Saha, S. Ghosh, and T. Kar (2011). Structural Elucidation and Electronic Properties of Two Pyrazole Derivatives: A Combined X-Ray, Hirshfeld Surface Analyses and Quantum Mechanical Study. *Chemical Physics Letters*, **506**(4-6); 309–314

Slodek, A., D. Zych, S. Kotowicz, G. Szafraniec-Gorol, S. Zimosz, E. Schab-Balcerzak, M. Siwy, J. Grzelak, and S. Maćkowski (2021). "Small in Size but Mighty in Force"– The First Principle Study of the Impact of A/D Units in A/D-Phenyl-π-Phenothiazine-π-Dicyanovinyl Systems on Photophysical and Optoelectronic Properties. *Dyes and Pigments*, **189**; 109248

Tawfik, S. M., A. Sayed, and I. Aiad (2012). Corrosion Inhibition by Some Cationic Surfactants in Oil Fields. *Journal of Surfactants and Detergents*, **15**(5); 577–585

Temma, A. S., O. N. Ali, R. H. Al-Asadi, and M. K. Mohammed (2025). Evaluation of Schiff Bases Against Two Cancer Cell Lines: A Combined Experimental and Theoretical Approach. *Tropical Journal of Natural Product Research*, **9**(3); 967–972

Xavier, S., S. Periandy, and S. Ramalingam (2015). NBO, Conformational, NLO, HOMO–LUMO, NMR and Electronic Spectral Study on *1-phenyl-1-propanol* by Quantum Computational Methods. *Spectrochimica Acta - Part A: Molecular and Biomolecular Spectroscopy*, **137**; 306–320